

Electroelastic fields in artificially created vortex cores in epitaxial BiFeO₃ thin films

B. Winchester, N. Balke, X. X. Cheng, A. N. Morozovska, S. Kalinin, and L. Q. Chen

Citation: [Applied Physics Letters](#) **107**, 052903 (2015); doi: 10.1063/1.4927750

View online: <http://dx.doi.org/10.1063/1.4927750>

View Table of Contents: <http://scitation.aip.org/content/aip/journal/apl/107/5?ver=pdfcov>

Published by the [AIP Publishing](#)

Articles you may be interested in

[Photovoltaic property of domain engineered epitaxial BiFeO₃ films](#)

Appl. Phys. Lett. **105**, 252903 (2014); 10.1063/1.4905000

[Coexistence of ferroelectric vortex domains and charged domain walls in epitaxial BiFeO₃ film on \(110\)O GdScO₃ substrate](#)

J. Appl. Phys. **111**, 104117 (2012); 10.1063/1.4722253

[X-ray nanodiffraction of tilted domains in a poled epitaxial BiFeO₃ thin film](#)

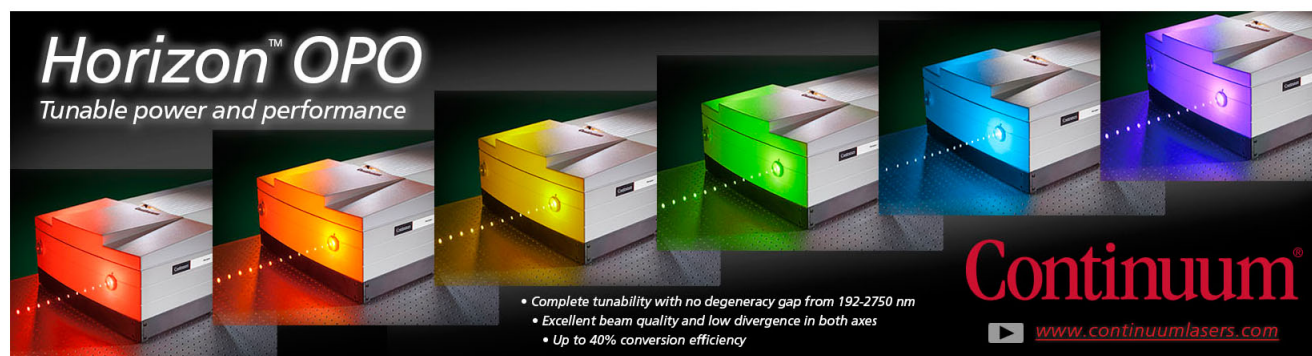
Appl. Phys. Lett. **99**, 232903 (2011); 10.1063/1.3665627

[Phase-field simulation of domain structures in epitaxial BiFeO₃ films on vicinal substrates](#)

Appl. Phys. Lett. **99**, 052903 (2011); 10.1063/1.3605674

[Switching kinetics in epitaxial BiFeO₃ thin films](#)

J. Appl. Phys. **107**, 084111 (2010); 10.1063/1.3392884



Horizon™ OPO
Tunable power and performance

- Complete tunability with no degeneracy gap from 192-2750 nm
- Excellent beam quality and low divergence in both axes
- Up to 40% conversion efficiency

Continuum®
www.continuumlasers.com

Electroelastic fields in artificially created vortex cores in epitaxial BiFeO₃ thin films

B. Winchester,^{1,a)} N. Balke,² X. X. Cheng,¹ A. N. Morozovska,³ S. Kalinin,² and L. Q. Chen¹

¹Department of Materials Science and Engineering, The Pennsylvania State University, University Park, Pennsylvania 16802, USA

²The Center for Nanophase Materials Sciences, Oak Ridge National Laboratory, Oak Ridge, Tennessee 37831, USA

³Institute for Problems of Materials Science, National Academy of Science of Ukraine, Kiev, Ukraine

(Received 16 April 2015; accepted 22 July 2015; published online 4 August 2015)

We employ phase-field modeling to explore the elastic properties of artificially created 1-D domain walls in (001)_p-oriented BiFeO₃ thin films, composed of a junction of the four polarization variants, all with the same out-of-plane polarization. It was found that these junctions exhibit peculiarly high electroelastic fields induced by the neighboring ferroelastic/ferroelectric domains. The vortex core exhibits a volume expansion, while the anti-vortex core is more compressive. Possible ways to control the electroelastic field, such as varying material constant and applying transverse electric field, are also discussed. © 2015 AIP Publishing LLC. [<http://dx.doi.org/10.1063/1.4927750>]

BiFeO₃ is a multiferroic with coupled antiferromagnetism ($T_N \approx 380^\circ\text{C}$) and ferroelectricity ($T_C \approx 820^\circ\text{C}$). The discovery of its high remanent polarization¹ in thin films has generated intense interest in the last few years for its potential applications in spintronics^{2,3} and non-volatile memory.⁴ It has recently been discovered that the domain walls in BiFeO₃ can be conductive.⁵ In particular, Balke *et al.*⁶ demonstrated the possibility of writing conductive domain channels into BiFeO₃ thin films through the introduction of topological defects in the domain structure. Here, we focus on the elastic fields at these topological defects and their effect on charge density distributions.

BiFeO₃ has a $R3c$ rhombohedral crystal structure, with polarization along the $\{111\}$ pseudocubic axes and thus eight symmetry-equivalent ferroelectric polarization states. Here, we denote the 8 rhombohedral polarization variants as $r_1^{+/-}$, $r_2^{+/-}$, $r_3^{+/-}$, and $r_4^{+/-}$, where the x-y components of the r^+ variants correspond to the four quadrants of the Cartesian coordinate system, and $r_i^- = -r_i^+$. A domain structure is made of regions of polarization states with different polarization directions. While the transition between two domains is called a domain wall, we will call the intersection of more than two domains a “junction,” and a 1-D domain junction a “core.”

In this paper, we examine two types of domain cores which run parallel to the $[001]_p$ direction. These are the intersections of the four r^+ variants: in the “vortex,” the in-plane polarizations of the surrounding domains rotate around the core (Fig. 1(a)), whereas the “anti-vortex” is comprised of the same four r^+ variants, arranged such that the in-plane polarizations alternate between pointing towards or away from the core (Fig. 1(b)). In experiment, these domain structures were constructed in BiFeO₃ films using SPM tip.^{6,7} Previously, we studied the conductive properties of the cores by their relation to the thermodynamic

equilibrium concentrations of oxygen vacancies, holes, and electrons in lightly doped materials.⁶ Since oxygen vacancies are coupled with strain through a positive Vegard stress coefficient in BiFeO₃ thin films, control of the elastic fields may offer some control of the conductance. Here, we employ phase-field modeling to study the elastic fields at the cores, with a discussion of varying material constant and applying transverse electric field, as possible ways to control the electroelastic field around the cores

We use the time-dependent Ginzburg-Landau (TDGL) equations to describe the evolution of the spatial polarization $\mathbf{P}(\mathbf{x}) = [P_1 P_2 P_3]$ over time

$$\frac{\partial P_i}{\partial t} = -L \frac{\delta F}{\delta P_i}, \quad (1)$$

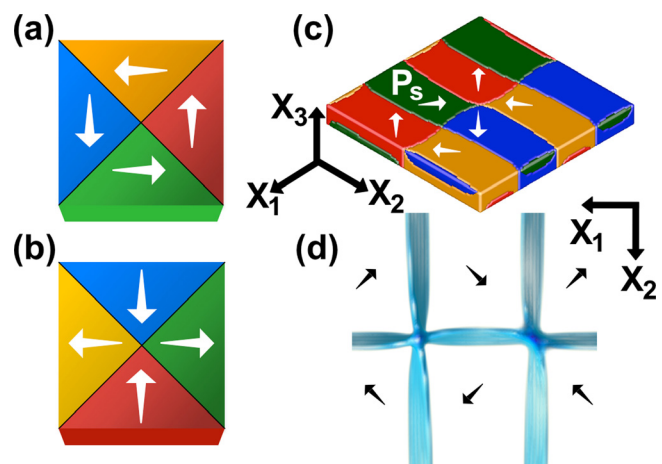


FIG. 1. A top-down schematic diagram of the (a) vortex and (b) anti-vortex cores, showing the relative directions of polarization in the four surrounding domains. Each of the domains has a positive out-of-plane polarization. (c) Perspective view of the starting simulation domain structure. (d) A top-down view of the domain walls at the vortex (left) and anti-vortex (right). Note that the domain wall twist at the vortex and the pinch at the anti-vortex vary through the height of the film, as each of the domain walls rotate to become parallel with $[001]$ near the core.

^{a)}E-mail: benjaminwinchester@gmail.com

where L is a kinetic parameter related to domain wall motion, P_i is the polarization field along axis x_i , and F is the total free energy functional, as given by the spatial integral of the Landau, gradient, electric, and elastic energy densities

$$F = \int_V (f_{\text{Landau}} + f_{\text{gradient}} + f_{\text{electric}} + f_{\text{elastic}}) dV. \quad (2)$$

We employ the polarization as the order parameter. The Landau, elastic, electrostatic, and gradient energy densities are written in terms of the polarization as follows.

The Landau energy density is

$$f_{\text{Landau}} = \alpha_1(P_1^2 + P_2^2 + P_3^2) + \alpha_{11}(P_1^4 + P_2^4 + P_3^4) + \alpha_{12}(P_1^2P_2^2 + P_2^2P_3^2 + P_1^2P_3^2), \quad (3)$$

where α_{ij} are the phenomenological Landau coefficients for a stress-free system and P_1 , P_2 , and P_3 are the polarization components in the x , y , and z direction. The gradient energy density is in the form of

$$f_{\text{gradient}} = \frac{1}{2} G_{ijkl} P_{i,j} P_{k,l}, \quad (4)$$

where $P_{i,j} = \partial P_i / \partial x_j$ and G_{ijkl} is the gradient energy coefficient, where G_{ijkl} is related to G_{mn} by Voigt's notation. We employ isotropic values for G_{mn} , where $G_{11} = 2G_{44}$ and $G_{12} = 0$. The elastic energy density is given by

$$f_{\text{elastic}} = \frac{1}{2} c_{ijkl} e_{ij} e_{kl} = \frac{1}{2} c_{ijkl} (\varepsilon_{ij} - \varepsilon_{ij}^0) (\varepsilon_{kl} - \varepsilon_{kl}^0), \quad (5)$$

where c_{ijkl} is the elastic stiffness tensor, $e_{ij} = \varepsilon_{ij} - \varepsilon_{ij}^0$ is the elastic strain, and ε_{ij}^0 and ε_{ij} denote the eigenstrains and the total strains, respectively. The film-substrate interface is assumed to be coherent. The eigenstrains are derived from the spontaneous ferroelectric structural transition by $\varepsilon_{mn}^0 = Q_{mnop} P_o P_p$, where Q is the electrostrictive coefficient. Finally, the electric energy density is given by⁸

$$f_{\text{electric}} = -E_i \left(\frac{1}{2} \varepsilon_b \varepsilon_0 E_i + P_i \right), \quad (6)$$

where ε_0 is the vacuum dielectric permittivity, ε_b is the background dielectric constant,^{9,10} and E_i is the total electric field.

More detailed descriptions of numerical methods employed in solving the evolution equations can be found in

the literature,^{11–13} and the elastic and Landau parameters used are listed in Ref. 14. We used a simulation size of $128 \Delta x \times 128 \Delta x \times 32 \Delta x$ with periodic boundary conditions. The film and substrate thicknesses were both set at $14 \Delta x$. The substrate is allowed to elastically deform down to the bottom boundary of the simulation box, where it is held fixed. The grid size Δx is related to the real size by $L_0 = \Delta x = \sqrt{G_{110}/\alpha_0}$, where $\alpha_0 = |\alpha_1|_{T=300\text{K}}$. We used a gradient energy coefficient of $G_{11}/G_{110} = 0.6$, which, if $L_0 = 1 \text{ nm}$, corresponds to a domain wall energy density of roughly 0.11 J/m^2 for a 71° domain wall.

We assumed a background dielectric constant of $\varepsilon_b = 50$ with short-circuit boundary conditions, fixed electric potential, on the top and bottom surfaces of the film. We assumed $T = 300 \text{ K}$, and we set the initial domain structure in rectangular domains similar to the experimental vortex/anti-vortex structure.

Fig. 1(c) shows the domain structure and the associated domain wall structure after the polarization evolution has stopped. We note that the domain structure at the top surface of the vortex core exhibits a twist opposite to the polarization rotation direction. Likewise, the top surface of the anti-vortex shows a ‘‘pinched’’ domain structure, where the outward-pointing domain variants grow at the expense of the inward-pointing domains, in agreement with experimental observations.⁶ These effects are reversed at the bottom surfaces. These ‘‘twist’’ and ‘‘pinch’’ effects are caused by the domain walls twisting away from their preferred $\langle 101 \rangle$ orientations¹⁵ to become parallel to $[001]$ near the cores. A cross-section across half the thickness of the film would show the four domain walls meeting at about 90° angles and running along the $[100]$ and $[010]$ axes. At the top and bottom of the film, however, the distortion results in the modified wall structure. For example, a wall between r_1^+ and r_4^+ with a preferred orientation of (101) will have an orientation of (100) at a core. For the vortex cores, this results in a clockwise rotation at the top of the film and a counterclockwise at the bottom of the film.

The vortex cores exhibit a high degree of in-plane elastic tensile strain ($\varepsilon_1 \approx 0.7\%$, $\varepsilon_2 \approx 1.1\%$), while the out-of-plane direction is compressively strained ($\varepsilon_3 \approx -0.4\%$), leading to volumetric expansion of about 1.4% along nearly the entire height of the core (Fig. 2(c)). The anti-vortex core exhibits much weaker volumetric compressive strains of about -0.1% ($\varepsilon_1 \approx -0.3\%$, $\varepsilon_2 \approx -0.6\%$, and $\varepsilon_3 \approx 0.9\%$).

TABLE I. Comparison of electrostatic potential ϕ and trace of stress tensor σ between anti-vortex core, vortex core, and control group (mid of domain), varying background dielectric constant ε_b , gradient energy coefficient g_{11} , and electrostrictive coefficient q_{44} . No change refers to original materials parameters, given in the text.

	Anti-vortex		Vortex		Control	
	ϕ	$\sum \sigma_{ii} (\times 10^8)$	ϕ	$\sum \sigma_{ii} (\times 10^8)$	ϕ	$\sum \sigma_{ii} (\times 10^8)$
No change	-0.19	-5.15	0.05	94.5	0.00	4.02
$\varepsilon_b = 25$	-0.20	-3.08	0.05	94.9	0.00	5.95
$\varepsilon_b = 100$	-0.18	-6.06	0.05	93.9	0.00	2.92
$g_{11} = 0.3$	-0.12	-13.8	0.08	94.0	0.00	3.76
$g_{11} = 1.2$	-0.18	3.00	0.04	90.0	0.00	4.23
$q_{44} = 0.0101$	-0.05	14.1	0.01	65.5	0.00	2.85
$q_{44} = 0.0403$	0.01	-7.79	0.34	90.4	0.00	8.37

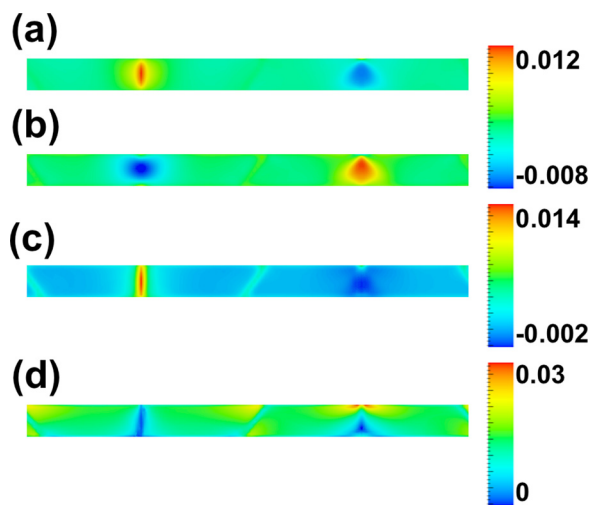


FIG. 2. Components of total strains: (a) $(\epsilon_{11} + \epsilon_{22})/2$, (b) (ϵ_{33}) , (c) $(\epsilon_{11} + \epsilon_{22} + \epsilon_{33})$, and (d) $(|\epsilon_{12}| + |\epsilon_{23}| + |\epsilon_{13}|)$, looking across $[1\ 1\ 0]$, with the vortex core visible on the left and the anti-vortex core on the right. Domain walls are visible on the sides and in the middle. The high in-plane expansion and out-of-plane compression of the vortex core is visible, with the resulting volumetric strain shown in (c). In (d), we note a decreased shear strain along the entire length of the vortex core, and mixed regions of high and low shear strain in the anti-vortex core.

The average out-of-plane polarization at the vortex core is $1.25p_0$ and $1.42p_0$ at the anti-vortex core, compared to $1.13p_0$ in the middle of a domain, while the in-plane polarizations at the cores are suppressed. The increased out-of-plane polarization at the cores is partially due to the fact that the core is the intersection of four domain walls between polarization variants with only $+P_3$ in common. We note that the increased P_3 is energetically expensive at the vortex core, given the local in-plane tensile strain. The strain properties of the cores are presented in Figure 2.

The interesting properties of the cores come from their symmetry-breaking or symmetry-enforcing structures. Each core type has its own local symmetry: in international notation, the anti-vortex core has symmetry mm^2 , with mirror planes at (110) and $(1\bar{1}0)$, while the vortex core has a symmetry of 4. In the domains surrounding the vortex core, the in-plane components of polarization are perpendicular to the core; so that with respect to the core, each domain has a negative ϵ_{12}^0 . That is, each of the neighboring domains exerts a tensile stress on the vortex core along the respective $\{1\ 1\ 0\}$ direction (Fig. 1(a)). Furthermore, at the center of the vortex core, the rotational symmetry is broken, and the shear strains $(\epsilon_{12}, \epsilon_{23}, \epsilon_{13})$ are suppressed (Fig. 2(d)). Based on these thoughts, we hypothesize that the elastic field at domain cores is mainly determined by the elastic properties in neighboring domains.

To test this hypothesis, we analyzed the volumetric strain at the cores and at the middle of a domain over a range of in-plane strain. Under a compressive strain, the polarization will rotate away from the plane of the film,¹⁴ which should decrease the ϵ_{12}^0 -related stresses around the vortex core. This was verified by our simulations, which showed a much greater change in volumetric strains over a range of mismatch strains from -1.0% to $+1.0\%$ at the vortex cores (see Fig. 3): a change of 1.8% for the vortex core, 0.95% for the anti-vortex core, and 1.1% for the middle of a domain.

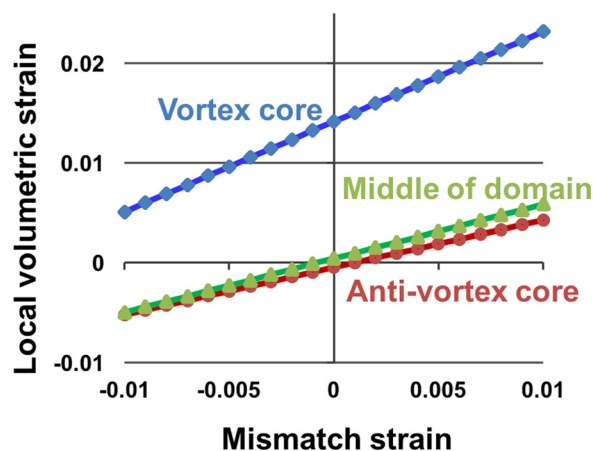


FIG. 3. Effect of mismatch strain on the local volumetric strain $(\epsilon_{11} + \epsilon_{22} + \epsilon_{33})$ at a vortex core (blue diamonds), anti-vortex core (red circles), and in the middle of a domain (green triangles). The volumetric strain of the vortex core is much more sensitive to changes in the applied strain, presumably due to the effect of the applied strain on the in-plane polarizations and eigenstrains.

Similarly, for the anti-vortex core, the in-plane polarization components in the surrounding domains point towards the core, resulting in a net in-plane compression and out-of-plane expansion of the core. In addition, the anti-vortex core also experiences the effects of the ϵ_{13}^0 shear strain component, which adds a thickness-dependent effect, and thus the properties show more variability through the thickness of the film. Overall, the anti-vortex core exhibits a more compressive in-plane strain compared to that of the vortex core, and P_3 is likewise higher here. The anti-vortex core also exhibits very high ϵ_{12} at the top surface. For the purpose of showing possible ways to control electroelastic fields at the cores, the effect of modified materials parameters and transverse electric field is explored (Table I).

In particular, we look at doubling and halving the dielectric constant ($\epsilon_b = 25$, $\epsilon_b = 100$), the normalized gradient energy coefficient ($g_{11} = 0.30$, $g_{11} = 1.20$), or the shear component of the electrostrictive coefficient ($q_{44} = 0.0403$, $q_{44} = 0.010075$).

We examine the background dielectric constant because it may affect the electric potential at the cores, and the value employed for BiFeO_3 under Landau theory has varied somewhat in the literature.^{16,17} The electrostrictive coefficient q_{44} is responsible for the elastic fields at the topological defects, as explained earlier and in the literature.^{18,19} Gradient energy coefficients g_{ij} is related to the domain wall energy, thus important for these 1D domain wall.

We find that the results vary little with respect to the background dielectric constant, at least, within the range of values examined here. Changes to the gradient energy coefficient cause moderate changes in electroelastic fields; the drop of about 0.05 V between the lower and upper values for g_{11} translates into an increase by a factor of ~ 10 in the concentrations of the oxygen vacancies or holes. Last, a drop in q_{44} does lead to the expected drop in segregation-inducing fields. However, we note an anomalously high potential for the vortex when q_{44} is doubled. As q_{44} is related to the degree of domain wall twist at the vortex cores via the ferroelastic distortion, and twisted domain walls are charged, we expect that the increase in potential is caused by the

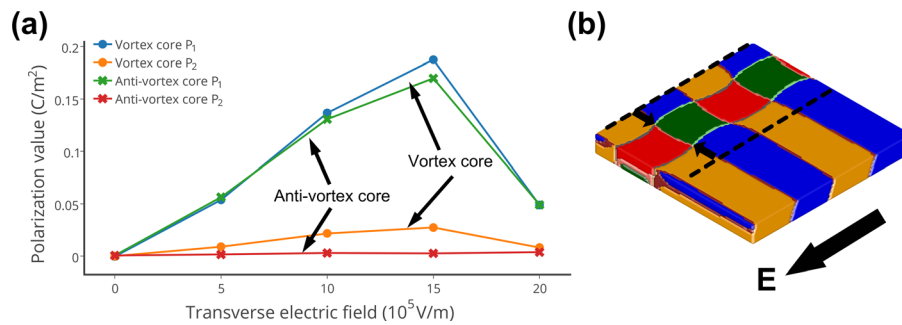


FIG. 4. (a) In plane polarization at vortex core and anti-vortex core under small transverse electric field in x direction. Polarization rotates at first, then after a threshold value, domain starts to grow or shrink. (b) In mid of evolution under 20 MV/m transverse electric field, the vortex cores and anti-vortex cores are moving towards each other and will finally disappear when reach the equilibrium state, white dashed lines marked the original positions of the cores.

increased domain wall twist. This also agrees with observations of the vortex core under an applied tip bias,⁶ in which applying a negative bias increased the (counterclockwise) domain twist, in order to form a compensating positive potential, and vice versa for positive bias case. Please refer to our previous publication⁶ for equations to calculate the equilibrium concentration of electrons, holes, and oxygen vacancies, and estimating the conductivity based on these information.

The effects of transverse electric field on cores come in two ways: first, shift the equilibrium value of the polarization, and second, change the fraction of different domains. Under relatively low transverse electric field, the vortex core and anti-vortex core will stay at the same position. With the increase of electric field, as it is shown in Fig. 4(a), the in plane polarization is aligning itself with the applied field in the x direction. The reason after a threshold value, polarization at the cores suddenly swing back, is because the cores start to move. Thus, minimization of free energy could also be achieved by increasing the portion of those domains whose direction is in congruent with the applied field. For our simulation system, this threshold value is between 1.5 MV/m and 2 MV/m. As illustrated in Fig. 4(b), favorable domains will grow larger.

When even higher field is applied, the simulation becomes a dynamic one, and it is hard to tell where the cores are and no simple rule could relate the polarization with the applied field. We found that under higher field, the migration speed of the cores has a linear relationship with the transverse electric field, but since our simulation time step is not mapped to time in real world, it is meaningless giving the fitted expression.

The electrostatic potential and volumetric stress vary little under different transverse field, mainly due to the small

value of the applied field (Table II). Similar to the polarization in Fig. 4(a), the trend of ϕ and $\sum\sigma_{ii}$ changes are different before and after the threshold. Though for the current simulation using different material (modifying the material constants) seems to be a more effective way of controlling the electroelastic field at cores than applying transverse electric field; in other cases, if we have the ability to pin the cores, such as dislocations, then higher transverse field could be applied and better control might be achieved.

The thermodynamic concentration of electrons (n), holes, and oxygen vacancies (N_V^+) is controlled by many factors including stress (σ_{ij}) and electrostatic potential (ϕ). The expressions are $n(r) = n_0 \exp(e\phi(r)/k_B T)$ and $N_V^+(r) = N_{V0}^+ \exp((\tilde{\beta}_{jk}^V \sigma_{jk}(r)/\rho - e\phi(r))/k_B T)$, where $\tilde{\beta}_{jk}^V$ is the Vegard stress tensor for oxygen vacancies, ρ is the number of atoms per unit volume in the material, e is the elementary charge, k_B is the Boltzmann's constant, and N_{V0}^+ and n_0 are the bulk concentrations of the oxygen vacancies and electrons, respectively.

Generally, the anti-vortex is characterized by a negative electric potential, which will lead to a competition between segregation of holes and oxygen vacancies, with holes dominant due to the low or negative stresses. The vortex, characterized by low but positive potentials and high positive stresses, will be characterized by a cooperative segregation of electrons and oxygen vacancies. These results agree with previous calculations,⁶ but under a much larger parameter space. The values here produce estimates of $10^1 - 10^3$ relative concentrations for holes at the anti-vortex. For the vortex cores, if we assume moderate cooperation between the electrons and oxygen vacancies such that the positive potential is completely screened by the electrons, and the stress is completely screened by the oxygen vacancies, we arrive at

TABLE II. Comparison of electrostatic potential ϕ and trace of stress tensor σ between anti-vortex core, vortex core, and control group (mid of domain), varying transverse electric field in x direction.

Transverse electric Field ($\times 10^5$ V/m)	Anti-vortex		Vortex		Control	
	ϕ	$\sum\sigma_{ii} (\times 10^8)$	ϕ	$\sum\sigma_{ii} (\times 10^8)$	ϕ	$\sum\sigma_{ii} (\times 10^8)$
0	-0.124	-2.69	0.431	87.3	0.004	2.74
5	-0.124	-2.71	0.434	87.0	0.004	2.70
10	-0.125	-2.83	0.442	86.0	0.004	2.66
15	-0.123	-2.94	0.441	85.1	0.004	2.62
20	-0.126	-2.69	0.438	87.0	0.004	2.57

similar estimates of relative defect concentrations of about $10^1 - 10^3$. High concentration of carriers at the cores directly leads to an increase of local conductivity, thus creating a conducting channel all the way through the film.

In summary, we conducted phase-field simulations to study the properties of a pair of topological defects in (001)_p-oriented BiFeO₃ thin films, the “vortex” and “anti-vortex” cores. We found that the vortex core is characterized by a strong tensile volumetric strain with repressed shear strains, while the anti-vortex core is characterized by a compressive volumetric strain and a mix of both enhanced and repressed shear strains, and volumetric strain at vortex core is more sensitive to mismatch strain compared with counterpart at anti-vortex core. We hypothesize that the elastic fields at the cores are largely governed by the elastic properties of the nearby domains. Behavior of polarization at the cores under transverse electric field is discussed. It is shown that using different material (changing related material constant) is a more effective way of influencing the electroelastic field at the cores, compared with applying a low transverse electric field. Future work on these topological defects should include investigation of the electrical switching properties, the effects of film thickness, and the effects of charged defects on the conductive properties.

The authors appreciate the financial support of the Department of Energy Basic Sciences under Grant No. DOE DE-FG02-07ER46417. N.B. and S.K. were supported by the Center for Nanophase Materials Sciences, which is a DOE Office of Science User Facility.

¹J. Wang, J. B. Neaton, H. Zheng, V. Nagarajan, S. B. Ogale, B. Liu, D. Viehland, V. Vaithyanathan, D. G. Schlom, U. V. Waghmare, N. A.

- Spaldin, K. M. Rabe, M. Wuttig, and R. Ramesh, *Science* **299**, 1719 (2003).
- ²H. Béa, M. Gajek, M. Bibes, and A. Barthélémy, *J. Phys.: Condens. Matter* **20**, 434221 (2008).
- ³G. Catalan and J. F. Scott, *Adv. Mater.* **21**, 2463 (2009).
- ⁴S. H. Baek, H. W. Jang, C. M. Folkman, Y. L. Li, B. Winchester, J. X. Zhang, Q. He, Y. H. Chu, C. T. Nelson, M. S. Rzhowski, X. Q. Pan, R. Ramesh, L. Q. Chen, and C. B. Eom, *Nat. Mater.* **9**, 309 (2010).
- ⁵J. Seidel, L. W. Martin, Q. He, Q. Zhan, Y. H. Chu, A. Rother, M. E. Hawkrige, P. Maksymovych, P. Yu, M. Gajek, N. Balke, S. V. Kalinin, S. Gemming, F. Wang, G. Catalan, J. F. Scott, N. A. Spaldin, J. Orenstein, and R. Ramesh, *Nat. Mater.* **8**, 229 (2009).
- ⁶N. Balke, B. Winchester, W. Ren, Y. H. Chu, A. N. Morozovska, E. A. Eliseev, M. Huijben, R. K. Vasudevan, P. Maksymovych, J. Britson, S. Jesse, I. Kornev, R. Ramesh, L. Bellaiche, L.-Q. Chen, and S. V. Kalinin, *Nat. Phys.* **8**, 81 (2012).
- ⁷N. Balke, S. Choudhury, S. Jesse, M. Huijben, Y. H. Chu, A. P. Baddorf, L. Q. Chen, R. Ramesh, and S. V. Kalinin, *Nat. Nanotechnol.* **4**, 868 (2009).
- ⁸M. Marvan and J. Fousek, *Phys. Status Solidi B* **208**, 523 (1998).
- ⁹D. C. Ma, Y. Zheng, and C. H. Woo, *Acta Mater.* **57**, 4736 (2009).
- ¹⁰A. K. Tagantsev, *Ferroelectrics* **375**, 19 (2008).
- ¹¹L. Q. Chen and J. Shen, *Comput. Phys. Commun.* **108**, 147 (1998).
- ¹²Y. L. Li, S. Y. Hu, Z. K. Liu, and L. Q. Chen, *Acta Mater.* **50**, 395 (2002).
- ¹³Y. L. Li, S. Y. Hu, Z. K. Liu, and L. Q. Chen, *Appl. Phys. Lett.* **81**, 427 (2002).
- ¹⁴J. X. Zhang, D. G. Schlom, L. Q. Chen, and C. B. Eom, *Appl. Phys. Lett.* **95**, 122904 (2009).
- ¹⁵S. K. Streiffner, C. B. Parker, A. E. Romanov, M. J. Lefevre, L. Zhao, J. S. Speck, W. Pompe, C. M. Foster, and G. R. Bai, *J. Appl. Phys.* **83**, 2742 (1998).
- ¹⁶M. Daraktchiev, G. Catalan, and J. F. Scott, *Phys. Rev. B* **81**, 224118 (2010).
- ¹⁷A. K. Tagantsev and G. Gerra, *J. Appl. Phys.* **100**, 051607 (2006).
- ¹⁸G. Arlt, *J. Mater. Sci.* **25**, 2655 (1990).
- ¹⁹G. Catalan, J. Seidel, R. Ramesh, and J. F. Scott, *Rev. Mod. Phys.* **84**, 119 (2012). The parameters (in SI units, where the temperature T is in °C) are as follows: $\alpha_1 = 8.78(T - 830) \times 10^5$, $\alpha_{11} = 4.71 \times 10^8$, $\alpha_{12} = 5.74 \times 10^8$, $Q_{11} = 0.035$, $Q_{12} = -0.0175$, $Q_{44} = 0.02015$, $c_{11} = 3.02 \times 10^{11}$, $c_{12} = 1.62 \times 10^{11}$, $c_{44} = 0.68 \times 10^{11}$.